

LEM2 and CHMP7 function in ESCRT-dependent nuclear envelope closure in yeast and human cells

Mingyu Gu^{1#}, Opal S. Chen^{1#}, Dollie LaJoie³, Mark S. Ladinsky⁴, Michael J. Redd⁵, Linda Nikolova⁶, Pamela J. Bjorkman⁴, Katharine S. Ullman³, Wesley I. Sundquist^{1*}, Adam Frost^{1,2*}

Affiliations:

¹ Department of Biochemistry, University of Utah, Salt Lake City, Utah 84112 USA

² Department of Biochemistry and Biophysics, University of California, San Francisco, San Francisco, CA, 94158 USA

³ Department of Oncological Sciences, Huntsman Cancer Institute, University of Utah, Salt Lake City, UT 84112

⁴ Cal-Tech Division of Biology and Biological Engineering, Caltech, Pasadena, CA, 91125 USA

⁵ HSC Imaging Core Facility, University of Utah, Salt Lake City, Utah 84122 USA

⁶ HSC Electron Microscopy Core Facility, University of Utah, Salt Lake City, Utah 84122 USA

These authors contributed equally to this work

To whom correspondence should be addressed:

wes@biochem.utah.edu (WIS) and adam.frost@ucsf.edu (AF)

Running Title:

ESCRT-dependent nuclear envelope closure

Keywords: LEM2/CHMP7/VPS4/ESCRT-III/nuclear envelope closure

Abstract

ESCRT-III proteins have been implicated in sealing the nuclear envelope in mammals, spindle pole body dynamics in fission yeast, and the clearance of defective nuclear pore complexes in budding yeast. Here, we report that Lem2p (LEM2), a member of the LEM (Lap2-Emerin-Man1) family of inner nuclear membrane proteins, and the ESCRT-II/ESCRT-III hybrid protein Cmp7p (CHMP7), collaborate to recruit ESCRT-III proteins to holes in the nuclear membrane. In fission yeast, deletion of the ATPase *vps4* leads to severe defects in nuclear morphology and integrity. These phenotypes are suppressed by loss-of-function mutations that arise spontaneously in *lem2* or *cmp7*, implying that all three function in the same pathway. In mammals, ESCRT factors participate in nuclear envelope reformation in anaphase, and we show that this process similarly depends on both LEM2 and CHMP7. Our observations suggest that Lem2p/LEM2 acts as a site-specific adaptor that recruits Cmp7p/CHMP7 and other ESCRT factors to the nuclear envelope.

Introduction

Fungal, plant, and animal genomes are isolated within the nucleus, an organelle with a boundary that comprises the double-membraned nuclear envelope (Devos et al., 2014). The inner and outer bilayers of the nuclear envelope are perforated by annular channels that contain Nuclear Pore Complexes (NPCs), each a massive assembly that regulates the trafficking of macromolecules like mRNA and proteins between the cytoplasm and nucleoplasm. The evolution of the envelope, among other roles, helped safeguard genome duplication and mRNA transcription from parasitic nucleic acids that compete for ribosomes in the cytosol (Madhani, 2013). The isolation of nucleoplasm from cytoplasm, however, presents a challenge during cell division when duplicated chromosomes must be separated for daughter cell inheritance.

Chromosome inheritance depends on assembly of a mitotic spindle, which pulls chromosomes toward opposite sides of the duplicating cell. Spindle assembly begins when two microtubule organizing centers (MTOCs) nucleate polymerization of anti-parallel arrays of microtubules in order to capture daughter chromosomes. Despite functional conservation throughout Eukarya, the mechanisms by which spindle microtubules breach the nuclear envelope to gain access to metaphase chromosomes vary markedly (Byers and Goetsch, 1975; Heath, 1980; Kubai, 1975; Tamm et al., 2011). In vertebrates and other Eukaryotes that have an “open mitosis”, the nuclear envelope opens up to such a degree that nucleoplasmic identity is lost. Certain protists and fungi, by contrast, maintain nuclear envelope integrity throughout mitosis in what is called a “closed mitosis” (Heath, 1980; Kubai, 1975).

The fission yeast *Schizosaccharomyces pombe* and the budding yeast *Saccharomyces cerevisiae* integrate their MTOC, known as the spindle pole body (SPB), into the nuclear envelope so that microtubule assembly can be catalyzed directly in the nucleoplasm (Byers and Goetsch, 1975; Ding et al., 1997; Heath, 1980; McCully and Robinow, 1971). In budding yeast,

duplication of the SPB is coupled with nuclear envelope remodeling so that mother and daughter SPBs reside within the envelope throughout the cell cycle (Adams and Kilmartin, 2000; Byers and Goetsch, 1975). Fission yeast, by contrast, restricts SPB access to the nucleoplasm during mitosis only (Ding et al., 1997; McCully and Robinow, 1971). Upon mitotic entry, a fenestration through the nuclear envelope opens transiently and the mother and the daughter SPBs are incorporated (Ding et al., 1997; Heath, 1980; Kubai, 1975; Tallada et al., 2009; Tamm et al., 2011). For every cell cycle, therefore, the fission yeast nuclear envelope opens and reseals twice: once when the SPB is ejected from the envelope following a successful cell cycle, and again when the SPBs are reinserted.

Incorporating NPCs and SPBs into the nuclear envelope requires certain factors and mechanisms in common, including membrane remodeling activities (Fischer et al., 2004; Jaspersen and Winey, 2004; Munoz-Centeno et al., 1999; Niepel et al., 2005; Tamm et al., 2011; Witkin et al., 2010). We and others reported strong genetic interactions between transmembrane nucleoporins, spindle pole body components, and endosomal sorting complexes required for transport (ESCRT) genes—portending a role for ESCRTs in nuclear membrane remodeling (Costanzo et al., 2010; Frost et al., 2012). ESCRT components are recruited to different target membranes by site-specific adaptors that ultimately recruit ESCRT-III subunits and their binding partners, including VPS4-family adenosine triphosphatases (ATPases) (Henne et al., 2011; Hurley, 2015; McCullough et al., 2013). We previously showed that certain ESCRT-III mutants and *vps4Δ* cells displayed an apparent over-amplification of SPBs (or defective fragments) in fission yeast (Frost et al., 2012), comparable to the centrosome fragmentation observed in human cells following depletion of VPS4 (Morita et al., 2010). We also reported that the severity of this SPB phenotype in fission yeast waned over time, suggesting possible genetic suppression (Frost et al., 2012). In budding yeast, Webster et al. reported that without ESCRT-III/Vps4 activity, misassembled NPCs accumulate in a

compartment they named the SINC for Storage of Improperly Assembled Nuclear Pore Complexes (Webster et al., 2014). They also showed that LEM family (Lap2-Emerin-Man1) inner nuclear membrane proteins, Heh1 and Heh2 in budding yeast, associate with defective NPC assembly intermediates (but not with mature NPCs), and that Heh1/2 proteins recruit ESCRT-III and Vps4 activities to malformed NPCs in order to clear them from the nuclear envelope (Webster et al., 2014).

Several recent reports have also demonstrated that certain ESCRT-III proteins and their associated ATPases are recruited transiently to gaps in re-forming mammalian nuclear membranes (Olmos et al., 2015; Vietri et al., 2015), and to rupture sites in the nuclei of interphase mammalian cells (Denais et al., 2016; Raab et al., 2016). For reforming nuclei in anaphase, depletion of ESCRT factors delays sealing of the nuclear envelope and impairs mitotic spindle disassembly (Olmos et al., 2015; Vietri et al., 2015). Vietri et al. showed that depletion of SPASTIN, a meiotic clade VPS4-family member and an ESCRT-III-binding enzyme (Monroe and Hill, 2015), delays spindle disassembly and prolongs ESCRT-III co-localization with re-forming envelope membranes (Vietri et al., 2015; Yang et al., 2008). Similarly, depletion of ESCRT-III impaired spindle disassembly, leading to a model in which certain ESCRT-III proteins and ATPases like SPASTIN coordinate microtubule severing with the closure of annular gaps in the nuclear envelope. This model is closely related to current thinking about cytokinetic abscission, where ATPases like SPASTIN disassemble the residual microtubules that pass between daughter cells, while ESCRT-III proteins constrict the midbody membrane to the point of fission (Connell et al., 2009; McCullough et al., 2013; Yang et al., 2008).

Vietri et al. also reported that a poorly-studied ESCRT-III-like protein, CHMP7, is required to recruit ESCRT pathway activities to the re-forming nucleus. Here we address the key question of what serves as the organelle-specific adaptor that facilitates CHMP7 recruitment

for its role in sealing annular gaps in the re-forming envelope. To identify factors in this pathway, we returned to the genetically tractable fission yeast system. We report that deletion of *vps4* in *S. pombe* leads to severe defects in nuclear membrane morphology, nuclear integrity, and secondary defects in NPCs and SPB dynamics. Remarkably, these phenotypes are suppressed spontaneously when cells acquire loss-of-function mutations in *cmp7*, ortholog of human CHMP7, or in *lem2*, a LEM family inner nuclear membrane protein and ortholog of human LEM2. We also show that in human cells recruitment of the ESCRT-III protein IST1 to the re-forming nuclear envelope depends on both LEM2 and CHMP7. Together, these observations implicate LEM2 as a nucleus-specific adaptor that recruits Cmp7p (CHMP7) and other ESCRTs to close the nuclear envelope during both open and closed mitoses.

Results

vps4Δ fission yeast cells grow very slowly and loss of either *cmp7* or *lem2* rescues growth

To determine whether and how our previously-reported *vps4Δ* phenotypes were suppressed over time (Frost et al., 2012), we monitored the growth rate of individual colonies following sporulation and tetrad dissection of *vps4Δ/+* diploid cells. Growth rates of *vps4Δ* spores were significantly slower than wild type spores (Fig 1A). This growth defect spontaneously reverted over time, so that when mutant spores were streaked on rich media, some *vps4Δ* colonies exhibited grow rates comparable with wild type colonies (Fig 1B). To identify potential suppressor mutations, we sequenced the whole genomes of 12 strains that spontaneously reverted to wild type growth rates and compared them to both wild type and apparently unsuppressed *vps4Δ* strains. Analysis of these genomes revealed that 7 out of the 12 suppressors had different loss-of-function mutations in the ESCRT-II/ESCRT-III hybrid gene, *cmp7* (Table EV1). The remaining 5 each had equivalent independent mutations in a LEM

domain family member, *lem2*, within what appears to be a slippery poly-T track (Table EV1). These 12 mutant alleles were further confirmed by Sanger sequencing and none of the suppressors were found to harbor mutations in both *cmp7* and *lem2*.

To determine whether these potentially suppressive alleles rescue the growth of *vps4Δ* cells, we engineered *cmp7Δ/+* and *lem2Δ/+* genotypes within our *vps4Δ/+* diploid background and isolated *lem2Δ*, *cmp7Δ*, *vps4Δ* single mutants and their corresponding double mutants via sporulation and tetrad dissection. Quantitative growth rates in liquid culture for biological and technical triplicates demonstrated that *cmp7Δ* single mutants had wild-type growth rates and, although the *vps4Δcmp7Δ* double mutant cells grew slightly slower than wild type cells, they grew much faster than *vps4Δ* single mutant cells (Fig 1C). Similarly, *lem2Δ* single mutants displayed a modest growth deficit compared to wild type, but *vps4Δlem2Δ* double mutant cells again grew much faster than *vps4Δ* cells (Fig 1C). Thus, our unbiased whole genome sequencing and targeted double mutant studies demonstrate that *cmp7* and *lem2* are bona fide *vps4* suppressors and the spontaneous mutations phenocopy null alleles.

vps4Δ cells have nuclear envelope defects which are suppressed by loss of *cmp7* or *lem2*

Next, we sought to discover the cellular defects that correlated with the slow growth of *vps4Δ* cells, and to test whether those defects were also rescued by *cmp7Δ* or *lem2Δ*. In light of our work on mitotic and spindle pole defects in *vps4Δ* cells, we first examined nuclear envelope (NE) and spindle pole body (SPB) morphology and dynamics. Over 80% of *vps4Δ* cells from recently-dissected *vps4Δ* haploid spores displayed severe NE morphology defects. These defects were rescued by loss of *cmp7* or *lem2* (Fig 2). Moreover, approximately 30% of *vps4Δ* cells displayed clearly asymmetric SPB segregation errors and anucleate daughter cells (Fig EV1A). Although loss of *cmp7* rescued these phenotypes, loss of *lem2* did not. In fact *lem2Δ* single mutant cells also displayed similar SPB segregation defects (Fig EV1B). Thus defects in

nuclear envelope morphology and integrity correlated with the slow growth phenotype, suggesting that these defects were primarily responsible for the *vps4Δ* slow growth phenotype.

vps4Δ cells display a series of mitotic errors associated with nuclear envelope defects

Live cell imaging using NE (Ish1p-mCherry) and SPB (Cut12p-YFP) markers enabled us to monitor the development and consequences of nuclear envelope defects in mutant versus wild type cells. Abnormal NE morphologies or asymmetric and even failed karyokinesis were observed in the majority of cells (Fig 3) and only ~30% of recorded *vps4Δ* cells displayed normal, symmetric karyokinesis (Fig 3A). An apparent proliferation or overgrowth of Ish1p-marked membranes, was a particularly common defect in *vps4Δ* cells. Approximately 25% of mutant cells displayed such long-lived NE “outgrowths” that we later determined were karmellae and related morphological defects (see below). The expanding karmellae regions usually formed near sites of SPB duplication, and the associated daughter SPBs in these cases often failed to separate normally or displayed extensive delays in separation (Fig 3B) Indeed, separation of duplicated SPBs was significantly prolonged in *vps4Δ* cells, whether or not they exhibited abnormal nuclear envelope malformations (Figure EV2). Together, these observations suggest that Vps4p plays a central role in regulating NE morphology in fission yeast, particularly during SPB extrusion or insertion through the NE, and perhaps also during karyokinesis.

vps4Δ nuclei leak and their integrity is partially restored by loss of *cmp7* or *lem2*

Our observations, together with recent reports that the ESCRT pathway closes holes in the mammalian nuclear envelope (Olmos et al., 2015; Vietri et al., 2015), prompted us to test the integrity of *vps4Δ* nuclei. In wild type cells, a large nuclear import cargo, NLS-GFP-LacZ, was confined strictly to the nuclear compartment with no detectable cytoplasmic signal, whereas approximately 30% of *vps4Δ* cells displayed clearly observable levels of cytoplasmic GFP, indicating loss of nuclear integrity (Fig 4A and B). Most mutant cells still showed some

enrichment of the cytoplasmic GFP reporter within the nucleus (Fig 4B, arrowhead), but some cells lost this enrichment completely (Fig 4B, arrow). Loss of *cmp7* or *lem2* largely rescued these nuclear integrity phenotypes (Fig 4C). We also noted a correlation between the extent of nuclear integrity loss and NE morphology defects using live cell imaging. Cells often displayed normal GFP reporter localization and normal NE morphology early during the experiment, but gradually accumulated cytoplasmic signal over the course of hours (Fig EV3A). Cells with grossly abnormal nuclear envelope morphology, by contrast, often lost GFP enrichment within the nucleus completely (Fig EV3B). These experiments further indicated that cytoplasmic GFP resulted from loss of nuclear integrity rather than from defects in nuclear import.

vps4Δ nuclear envelopes are persistently fenestrated and have karmellae and disorganized tubular extensions

We employed electron tomography of high-pressure frozen and freeze-substituted cells to examine whether we could detect morphological defects in the nuclear envelope that could account for the loss of nuclear integrity. Serial 400nm sections were imaged and reconstructed to generate 3D volumes of >1 micron thickness. Wild type nuclei had evenly spaced inner and outer lipid bilayers with embedded nuclear pore complexes evenly distributed around the periphery (Fig 5A and Movie EV1). *vps4Δ* nuclei, by contrast, displayed at least four structural abnormalities. First, large fenestrations through both the inner and outer nuclear membranes were observed (Fig 5B, bracket). Second, karmellae or concentric layers of membrane were present around certain regions of the mutant nuclei (Fig 5B arrowheads). Third, extensive whorls of disorganized tubulo-vesicular membranes that were topologically continuous with the adjacent karmellae were apparent (Fig 5B, arrows and Figure EV4). Fourth, the total number of NPCs appeared to be decreased (Fig 5B, asterisk) and the NPCs that were present were localized in regions that were free of karmellae and tubulo-vesicular structures (Fig 5D). 3D reconstruction of these features confirmed the presence of very large gaps (>400nm) in the

nuclear envelope and topologically continuous karmellae and whorls of tubular extensions (Fig 5C and Movie EV2 to 4). Persistent fenestrations explain the loss of nuclear integrity in *vps4Δ* cells, while karmellae and other disorganized extensions may underlie the kinetic delays, asymmetries, and outright failures of SPB separation and karyokinesis.

vps4Δ nuclear envelope defects are suppressed by loss of *cmp7* or *lem2*

Thin section electron microscopy of single and double mutant cells demonstrated that karmellae formation in *vps4Δ* cells was completely suppressed by loss of *cmp7* or *lem2* (Fig 6). Remarkably, these double mutant cells displayed wild-type like nuclei, although a few examples of nuclear fenestrations were observed in *lem2Δ* single mutant cells (Fig 6G). These observations indicate that in the absence of Vps4p, karmellae formation depends on both Lem2p and Cmp7p. In fact, overexpressing Lem2p in *S. pombe*, or compromising nuclear import of Heh2p, the orthologue of Lem2p in *S. cerevisiae*, induces the formation of similar abnormalities (Gonzalez et al., 2012; King et al., 2006). Together, these results suggest that abnormal Lem2p activity drives the formation of nuclear envelope malformations via a pathway that also requires Cmp7p.

Depletion of LEM2 or CHMP7 in human cells prevents ESCRT-III recruitment to the reforming nuclear envelope during anaphase

LEM2 and its homologs are two-pass membrane proteins that are normally imported through the NPC and restricted to the inner nuclear membrane (King et al., 2006). The homolog in budding yeast, Heh2, has been previously implicated in ESCRT-dependent repair of defective NPCs (Webster et al., 2014). This study, together with our observations, suggested that LEM2-like proteins in both budding and fission yeast may be site-specific nuclear membrane adaptors for the ESCRT pathway that specifically recruit or activate Cmp7p/CHMP7 proteins to close holes in the nuclear envelope. To test the generality of this model, we tested whether LEM2

(encoded by the *LEMD2* gene) and CHMP7 are required for IST1 recruitment to anaphase chromatin in human cells (Fig 7). IST1 is an ESCRT-III protein that is specifically recruited to condensed chromatin discs to promote coordinated NE closure and disassembly of spindle microtubules in human cells (Vietri et al., 2015). To enrich for cells in anaphase, HeLa cells were first synchronized in G1/S by thymidine treatment. 12 hours after release (Fig 7A), cells progressed into mitosis where IST1 formed discrete puncta, frequently in two discernable strips, at chromatin discs during anaphase B (Fig 7). siRNA-mediated depletion of CHMP7 abrogated IST1 recruitment to chromatin, consistent with the previously observed role for CHMP7 in the recruitment of CHMP4B to assembling nuclei (Vietri et al., 2015). siRNA-mediated depletion of LEM2 also strongly attenuated IST1 recruitment (Fig 7C, D), although the phenotype was less severe than that seen for CHMP7 depletion. Thus, both LEM2 and CHMP7 are required to recruit additional ESCRT-III machinery, including IST1, to the reforming nuclear envelope during anaphase and these nuclear-membrane remodeling activities are conserved from yeast to human cells.

Discussion

Pioneering work on the ESCRT pathway in budding yeast led to our understanding of its roles in multi-vesicular body biogenesis (Henne et al., 2011), while work in human cells led to a broader view of ESCRT roles at a diversity of target membranes (Hurley, 2015). Our prior work in fission yeast and results reported here indicate that the role of the ESCRT pathway in closing holes in the nuclear envelope is evolutionarily ancient (Frost et al., 2012). The different nuclear ESCRT functions (NPC surveillance, nuclear envelope reformation, and SPB insertion/removal) can now be unified by the hypothesis that all of these processes generate fenestrations in the nuclear envelope that must be closed by the ESCRT pathway (Campsteijn et al., 2016; Denais et al., 2016; Olmos et al., 2015; Raab et al., 2016; Vietri et al., 2015; Webster et al., 2014). Conserved activities include roles described in this work for nucleus-specific adaptors of the

LEM domain family and the ESCRT-II/ESCRT-III hybrid protein, CHMP7/Cmp7p (Bauer et al., 2015; Webster et al., 2014). This conserved pathway may likewise underlie the requirement for Src1, a LEM-domain protein in *A. nidulans*, in formation of stable nuclei (Liu et al., 2015).

In *S. cerevisiae* there are two LEM family members involved in ESCRT recruitment, Heh1 and Heh2, so multiple LEM family proteins may be involved in recruiting ESCRT-III activities in mammalian cells as well. In this regard, knockdown of LEM2 in HeLa cells led to a less severe phenotype than knockdown of CHMP7 in our work—thus it will be of great interest to determine whether CHMP7/Cmp7p proteins have some inherent ability to target nuclear membranes or whether other LEM-domain family members also serve as recruitment factors in human cells. It will also be important to determine the mechanistic basis of our *vps4Δ* phenotypes and the toxicity of unrestricted Lem2p-Cmp7p pathway activity. We propose that in the absence of Vps4p, Lem2p-Cmp7p may together stabilize nuclear membrane fenestrations aberrantly or promote nuclear envelope remodeling events that—when unregulated by Vps4p—result in karmellae and other malformations that ultimately compromise cell growth. Overexpression of Lem2p in fission yeast induces nuclear envelope malformations (Gonzalez et al., 2012); and if nuclear import of Heh1/2p is compromised in budding yeast, karmellae develop (King et al., 2006). Both of these phenotypes likely depend on CHMP7/Cmp7p proteins and other downstream ESCRT pathway activities. Studies of these and related activities in the future will benefit from the facile *S. pombe* genetic system for investigating how the ESCRT pathway senses and seals perforations through the nuclear envelope.

Materials and Methods

Yeast strains and growth media

S. pombe, diploid strain SP286 (*h+*/*h+*, *leu1-32/leu1-32*, *ura4-D18/ura4-D18*, *ade6-M210/ade6-M216*) was used for all haploid constructions. All other strains used in this study are

listed in Appendix Table S1. Cells were routinely grown in YE5 rich media (yeast extract 0.5% w/v, glucose 3.0% w/v supplemented with 225 mg/L histidine, leucine, uracil and lysine hydrochloride and 250 mg/L adenine) or Edinburgh Minimal Media (EMM, Sunrise Sciences Products) with supplements described above (EMM5). Sporulation of diploids was induced by culturing cells in EMM5 without glutamate (EMMG, Sunrise Sciences Products) and supplemented as above but without uracil. Dominant drug selection was performed with YE5 supplemented with G418 disulfate (KSE Scientific) at 200 mg/L, hygromycin B, *Streptomyces*, sp. (Calbiochem) at 100 mg/L and ClonNAT at 100 mg/L. To prevent caramelization, YE5 was routinely prepared by leaving out glucose during autoclaving and adding it before inoculation.

Yeast transformation

Log phase yeast cells were incubated in 0.1M Lithium Acetate (pH 4.9) for 2 hours, at a concentration of 5×10^8 cells/ml. 100 μ l of this cell suspension was then mixed with 0.5-1 μ g DNA and 290 μ l 50% PEG8000 and incubated overnight. Cells were recovered in 0.5X YE5 medium overnight before plating. All steps were conducted at 32°C.

Sporulation, random spore analysis and tetrad dissection

Sporulation of *S. pombe* diploids for tetrad dissection or random spore analysis was induced by first transforming pON177 (*h*- mating plasmid with *ura4* selectable marker, a gift from Megan King, Yale School of Medicine) into the parental strain. Transformants were selected on EMM5 without uracil (EMM5-uracil) for three days at 32°C followed by induction in 0.5 ml EMMG without uracil (EMMG-uracil) for 36 to 48 hours at 25°C. Sporulation was confirmed by microscopy. Ascus walls of tetrads were digested with 2% (v/v) β -glucuronidase (Sigma-Aldrich) overnight at 25°C. This overnight treatment also eliminated non-sporulated diploids. Enrichment of spores was verified by microscopy. Five to 10 fold serial dilutions were made and spores were plated on YE5 supplemented with specific antibiotics.

Tetrad dissection: 10-fold serial dilutions of β -glucuronidase-treated tetrads were placed onto YE5 plates as a narrow strip and digestion was monitored at room temperature. Tetrads were picked and microscopically dissected along pre-designated lines of the same YE5 plate. Spores were allowed to germinate and grow at 32°C.

Knockout cassettes and plasmids

vps4 deletion cassette: the *vps4Δ::natMX6* template (Frost et al., 2012) was amplified to create an amplicon covering 756 bp upstream of the ATG and 499 bp downstream of the stop codon. This 2439 bp amplicon was transformed into SP286 and plated on YE5 + ClonNAT to select for heterozygous *vps4Δ::natMX6/+* diploids.

cmp7 deletion cassette: a fragment including 420 bp upstream of the ATG and 377 bp downstream of the stop codon was amplified and cloned into BamHI/BglII and EcoRV/SpeI of pAG32 (a pFA6 derived plasmid containing *hphMX4* which confers resistance to hygromycin B, a gift from David Stillman, Department of Pathology, University of Utah). The *cmp7Δ::hphMX4* fragment was amplified and transformed into heterozygous *vps4Δ::natMX6/+* diploid intermediate strain and selected on YE5 supplemented with both ClonNAT and hygromycin B.

lem2 deletion cassette: a 3.1 kb *lem2* genomic fragment spanning 600 bp upstream of the ATG to 500 bp downstream of the stop codon, was subcloned into pGEM vector. The ORF region was replaced with a *hphMX4* hygromycin resistance cassette to make the final knock-out construct (pMGF130). The *lem2Δ::hphMX4* cassette was amplified and transformed into heterozygous *vps4Δ::natMX6/+* diploids and selected on YE5 supplemented with both ClonNAT and hygromycin B.

cut12-YFP cassette: a 3.5 kb synthetic DNA fragment was created that spanned 550 bp C-terminal of *cut12* fused with *YFP* followed by *kanMX6* and a 500 bp fragment downstream of the

cut12 stop codon. The fragment was transformed into heterozygous diploid strains and the resulting diploids were selected on YE5 supplemented with G418 disulfate.

ish1-mCherry cassettes: a 1kb *ish1* genomic DNA fragment corresponding to 500 bp upstream and 500 bp downstream of the *ish1* stop codon was subcloned into the pGEM vector. A flexible linker (GGTGGSGGT) and *mCherry* fusion cassettes were assembled, followed by the *yADH1* terminator and MX4/6 drug resistance or auxotrophic markers. These cassettes were integrated at the native *ish1* locus to make the final fusion constructs: *ish1-mCherry::natMX6* (pMGF170), *ish1-mCherry::kanMX6* (pMGF169), *ish1-mCherry::hphMX4* (pMGF157) and *ish1-mCherry::ura4(+)* (pMGF172).

pDual-SV40NLS-GFP-LacZ construct: a *SV40NLS-GFP-LacZ* fragment was amplified from pREP3X (provided by Dr. Shelley Sazer, Baylor College of Medicine) and subcloned downstream of the *Pnmt1* promoter in the *pDual* vector. The final construct (pMGF173) was integrated at the *leu1* locus.

Isolation of *vps4Δ* and suppressors

Isolation and handling of *vps4Δ* haploids: individual petite colonies from random spore analysis plates of YE5+ClonNAT were selected, re-suspended in 200 μL YE5 media, plated onto two YE5+ClonNAT plates and incubated at 32°C for three days. Isolates that grew across one plate without apparent suppression were frozen with glycerol without further culturing by scraping and re-suspension in YE5 with 15% glycerol. Cells from the other plate were scraped and genomic DNA was immediately extracted for Illumina sequencing.

Isolation of *vps4Δ* suppressors: *vps4Δ* isolates were re-streaked from glycerol stocks and cultured on YE5 at 32°C. Large colonies (apparent suppressors) were picked, re-suspended in 200 μL YE5 media and plated onto two YE5 plates. After two days, cells were harvested as described above for glycerol stocks and genomic DNA extraction.

Yeast genomic DNA extraction, Illumina sequencing and analysis

Genomic DNA extraction: frozen pellets of *wt*, *vps4Δ* or suppressor cells (200 μl) were thawed on ice. 250 μL resuspension buffer (20 mM Tris-HCl, pH 8.0, 100 mM EDTA, 0.5 M β-mercaptoethanol) and 50 μL lyticase (50 units)) were then added to remove the cell wall. Genomic DNA was extracted using phenol/chloroform/isoamyl alcohol, precipitated with ethanol and treated with RNase, followed by DNeasy Blood Tissue purification according to the manufacturer's protocol (Qiagen cat. 69504).

Illumina sequencing: libraries were constructed using the Illumina TruSeq DNA Sample Preparation Kit (cat. no. FC-121-2001, FC-121-2002) as described below. Briefly, genomic DNA was sheared in a volume of 52.5 μl using a Covaris S2 Focused-ultra-sonicator with the following settings: Intensity 5.0; Duty cycle 10%; Cycles per Burst 200; Treatment Time 120 seconds. Sheared DNA was converted to blunt-ended fragments and size selected to an average length of 275 bp using AMPure XP (Beckman Coulter cat. no. A63882). Following adenylation of the DNA, adapters containing a T-base overhang were ligated to the A-tailed fragments. Adapter ligated fragments were enriched by PCR (8 cycles) and purified with AMPure XP. The amplified libraries were qualified on an Agilent Technologies 2200 TapeStation using a D1K ScreenTape assay (cat. no. 5067-5363) and quantitative PCR was performed using the Kapa Biosystems Kapa Library Quant Kit (cat. no. KK4824) to define the molarity of adapter-modified molecules. Molarities of all libraries were subsequently normalized to 10 nM and equal volumes were pooled in preparation for Illumina sequencing.

Sequencing data analysis: raw reads were aligned to the *S. pombe* genome, obtained from Ensembl Fungi, using NovoCraft Novoalign and allowing for no repeats (-r None) and base calibration (-k). Alignments were converted to the Bam format using samtools (<http://samtools.sourceforge.net>). Sequence pileups were generated with the samtools pileup

function, and variants called using the bcftools utility (options -c -g -v). Variants were filtered using the included varFilter Perl script included with samtools and written out as a vcf file. To distinguish unique variants in each strain from common variants, sample vcf files were intersected with one another using the Perl script intersect_SNPs (<https://github.com/tiparnell>). Variants were annotated with the Perl script locate_SNPs (<https://github.com/tiparnell>) using a GFF3 gene annotation file obtained from Ensembl. From the resulting table, variants were further filtered by the fraction of reads supporting the alternate allele, the presence of codon changes, and visual inspection in a genome browser. The summary statistics are reported in Table EV1.

Fluorescence microscopy

All yeast strains were cultured in either YE5 or in EMM5 if the desired protein was induced by the *nmt1* promoter. Cells were imaged after reaching log phase. Hoechst staining was conducted at 1µg/ml in water for 15 minutes. Images were collected on a Zeiss Axio Observer Z1 microscope using a 100X oil-immersion objective.

HeLa cells were fixed in -20°C methanol for 10 minutes. The primary antibodies used for immuno-detection were rabbit α-IST1 (Bajorek et al., 2009) and rat α-tubulin (YL1/2; Accurate Chemical & Scientific, Westbury, NY). Following incubation with fluorescently labeled secondary antibodies (Thermo Fisher), coverslips were mounted using DAPI ProLong Gold (Thermo Fisher) and imaged. For the purpose of illustration, images of anaphase B cells were acquired by spinning disk confocal microscope and adjusted so that cytoplasmic IST1 intensity was comparable between samples. Images acquired by widefield microscopy at 100X were used to score the IST1 phenotype following minimal adjustment that was applied uniformly. IST1 localization to anaphase B chromatin masses was assessed in three independent experiments. Each chromatin disc (two per cell) was scored as having either robust, weak or no IST1

recruitment. Robust IST1 recruitment was characterized by distinctive foci organized at chromatin masses while weak IST1 recruitment was characterized by less intense, often fewer and less organized foci at the chromatin surface. Images of 188 anaphase B cells from all treatments and experiments were randomized and quantified blindly by three scorers. Final scores were also assigned blindly; the majority score was used in cases where the three scores differed.

Time-lapse light microscopy analysis

Wild type and *vps4Δ* cells were grown in YE5 at 32°C for 8 hours and loaded into the CellASIC ONIX Microfluidic system (Cat. EVE262, EMD Millipore), which immobilizes the cells in a single focal plane, maintains a constant temperature (32°C) and pumps fresh media over the cells. Images from multiple positions per chamber were captured every 10 minutes for 16 hours. A lens heater was used to maintain constant temperature inside the chamber. Images were collected with an Andor Clara CCD camera attached to a Nikon Ti microscope using a 60x oil Nikon Apo Lambda S NA 1.4 lens. The samples were illuminated with a Lumencor Sola LED at 20% intensity, which was further reduced by the insertion of an ND8 filter. Exposure times ranged between 1 to 3 seconds for both YFP and mCherry channels. Five Z plane images separated by 1 micron were collected. Maximum intensity projection images were created to follow the Cut12p-YFP signals within a given cell. For Ish1p-mCherry signals, only the Z plane that bisected the nucleus was chosen for further image analysis.

Electron microscopy

Yeast strains were grown to log phase and harvested using gentle vacuum filtration onto filter paper. The cell pellet was scraped from the filter, mixed with cryo-protectant (20% BAS in PBS), transferred to the well of a 100 μm specimen carrier (type A), and covered with the flat side of a type B specimen carrier (McDonald and Auer, 2006). The loaded specimens were

immediately frozen with a high-pressure freezer (EM-HPM100; Leica Microsystems, Vienna). Frozen cell were transferred for freeze-substitution (FS) to a pre-cooled Leica AFS unit (Leica Microsystems) and processed in the following substitution solution: 97% anhydrous acetone (EMS, RT10016) and 3% of water, 2% osmium tetroxide and 0.1% uranyl acetate. Substitution started at -90°C for 72 hours followed by a gradual increase in temperature (5°C/hr) to -25°C over 13 hours, held at -25°C for 12 hours, then warmed (10°C/hr) to 0°C over 2.5 hours). The samples were removed from the AFS unit, washed 6 times with pure acetone, and gradually infiltrated and embedded in Epon12-araldite resin as follows: 50% epon12-araldite/acetone overnight, 75% epon12-araldite/acetone for 24 hours, 100% epon12-araldite for 8 hours and polymerized at 60°C for 48 hours. Ultrathin sections (70 nm) were cut using a diamond knife (Diatome, Switzerland), using a UC6 microtome (Leica Microsystems), transferred to Formvar- and carbon-coated mesh copper grids (Electron Microscopy Sciences, FCF-200-Cu) and post-stained with 3% uranyl acetate and Reynold's lead citrate. The sections were viewed with a JEM-1400 Plus transmission electron microscope (JEOL, Ltd, Japan) at 120 kV and images collected on a Gatan Ultrascan CCD (Gatan Inc., Pleasanton CA).

Electron tomography

Blocks of embedded *wt* and *vps4Δ* *S. pombe* cells were trimmed to $\sim 100 \times 200 \mu\text{m}$ faces. Serial semi-thick (400 nm) sections were cut with a UC6 ultramicrotome (Leica Microsystems) using a diamond knife (Diatome Ltd. Biel, Switzerland). Ribbons of 10-20 sections were placed on Formvar-coated, copper-rhodium 1 mm slot grids (Electron Microscopy Sciences, Fort Washington PA) and stained with 3% uranyl acetate and Reynold's lead citrate. Colloidal gold particles (10 nm) were placed on both surfaces of the sections to serve as fiducial markers for subsequent tomographic image alignment and the grids carbon coated to enhance stability in the electron beam.

Grids were placed in a dual-axis tomography holder (Model 2040; EA Fischione Instruments, Inc., Export, PA.) and imaged with a Tecnai TF30-ST transmission electron microscope (FEI Company, Hillsboro, OR) equipped with a field emission gun and operating at 300KeV. Well-preserved cells displaying structures of interest were identified and tracked over 6-10 serial sections. The volume of the cell present in each section was then imaged as a dual-axis tilt series; for each set, the grid was tilted +/- 64° and images recorded at 1° intervals. The grid was then rotated 90° and a similar series recorded about the orthogonal axis. Tilt-series datasets were acquired automatically using the SerialEM software package (Mastronarde, 2005) and images recorded with a XP1000 CCD camera (Gatan Inc., Pleasanton CA). Tomographic data was calculated and serial tomograms were joined together using the IMOD software package (Diez et al., 2006; Kremer et al., 1996; Mastronarde, 2008). Tomograms were analyzed, segmented and modeled using IMOD. The nuclear envelope was traced with closed contours in each tomogram. Modeled contours were smoothed and 3D surfaces generated with tools in the IMOD software package. The “Z inc” value was set to 3 for all nuclear envelope objects to further smooth their surface. The number of serial semi-thick (400nm) sections used for model segmentation and display were: 3 for *wt* (Movie EV1); 2 for *vps4Δ* (Movie EV2); 4 for *vps4Δ* (Movie EV3) 3 for the second *vps4Δ* (Movie EV4).

siRNA-mediated depletion and cell cycle synchronization.

HeLa cells were plated on fibronectin-coated coverslips in the presence of 10 nM siRNA oligo, delivered by Lipofectamine RNAiMAX Transfection Reagent (Thermo Fisher). Specific sequences used were: siControl [siScr-1; (Mackay et al., 2009)], siLEM2-1 [antisense sequence targeting nucleotides 78-98: UUGCGGUAGACAUCCCGGGdTdT; (Ulbert et al., 2006)], siLEM2-2 [antisense sequence targeting nucleotides 1008-1028: UGGUCUUCUCCUUUCAACCDdTdT; (Ulbert et al., 2006)], siCHMP7-1 [CHMP7 650; sense sequence: GGGAGAAGAUUGUGAAGUdTdT; (Morita et al., 2010)], and siCHMP7-2 [CHMP7 613; sense

sequence: CAGAAGGAGAAGAGGGUCAdTdT; (Morita et al., 2010)]. After 8 hours, 2 mM thymidine was added to the media for 24 hours to arrest cells at G1/S. Cells were then rinsed thoroughly with PBS followed by the addition of culture media. Twelve hours after release, cells were fixed for microscopy. To verify efficacy and specificity of siRNA treatments, HeLa cells were plated in 6-well dishes and subjected to similar conditions as above. Cell lysates were then harvested and 5 µg of each lysate analyzed with immunoblots. Following incubation with primary antibodies (α-LEM2 (HPA017340; Sigma), α-CHMP7 (HPA036119; Sigma), α-tubulin (YL1/2)), reactivity was detected using HRP-coupled secondary antibodies (Thermo Fisher) and chemiluminescence.

Acknowledgements

We thank Dr. Brian Dalley and Dr. Tim Parnell for advice and expertise in whole genome sequencing and analysis, Dr. Mark Smith for assistance with confocal microscopy, Dr. Doug Mackay for advice, Dr. Shelley Sazer for a NLS-GFP-LacZ nuclear integrity reporter, Dr. Yasushi Hiraoka for an Ish1-GFP strain, and Dr. Patrick Lusk for stimulating conversations about unpublished results. Light and 2D transmission electron microscopy were performed in the Health Sciences Cores at the University of Utah. Microscopy equipment was obtained using a NCRR Shared Equipment Grant 1S10-RR024761-01. Our research was also supported by the Searle Scholars Program (A.F.), NIH 2P50-GM082545-06 (W.I.S., A.F., M.S.L., and P.J.B.), 1DP2-GM110772-01 (A.F.), 1R01-GM112080 (W.I.S.), the Huntsman Cancer Foundation and the Huntsman Cancer Institute Cancer Center Support Grant NIH P30CA042014 (K.S.U., W.I.S., A.F. and the Genomics and Bioinformatics Shared Resource).

Author Contributions

AF and WIS designed the project. DL performed human cell siRNA experiments. ML collected data for *S. pombe* electron tomography. MR helped to perform *S. pombe* living cell imaging. LN helped to perform *S. pombe* high pressure freezing and freeze substitution. MG and OSC performed all other experiments. MG, OSC, AF, and WIS analyzed the data. MG, OSC, AF and WIS wrote the paper.

Conflict of Interest

The authors declare that they have no conflict of interest.

References

- Adams, I.R., and Kilmartin, J.V. (2000). Spindle pole body duplication: a model for centrosome duplication? *Trends in cell biology* *10*, 329-335.
- Bajorek, M., Morita, E., Skalicky, J.J., Morham, S.G., Babst, M., and Sundquist, W.I. (2009). Biochemical analyses of human IST1 and its function in cytokinesis. *Molecular biology of the cell* *20*, 1360-1373.
- Bauer, I., Brune, T., Preiss, R., and Kolling, R. (2015). Evidence for a Nonendosomal Function of the *Saccharomyces cerevisiae* ESCRT-III-Like Protein Chm7. *Genetics* *201*, 1439-1452.
- Byers, B., and Goetsch, L. (1975). Behavior of spindles and spindle plaques in the cell cycle and conjugation of *Saccharomyces cerevisiae*. *Journal of bacteriology* *124*, 511-523.
- Campsteijn, C., Vietri, M., and Stenmark, H. (2016). Novel ESCRT functions in cell biology: spiraling out of control? *Current opinion in cell biology* *41*, 1-8.
- Connell, J.W., Lindon, C., Luzio, J.P., and Reid, E. (2009). Spastin couples microtubule severing to membrane traffic in completion of cytokinesis and secretion. *Traffic* *10*, 42-56.
- Costanzo, M., Baryshnikova, A., Bellay, J., Kim, Y., Spear, E.D., Sevier, C.S., Ding, H., Koh, J.L., Toufighi, K., Mostafavi, S., *et al.* (2010). The genetic landscape of a cell. *Science (New York, NY)* *327*, 425-431.
- Denais, C.M., Gilbert, R.M., Isermann, P., McGregor, A.L., Te Lindert, M., Weigelin, B., Davidson, P.M., Friedl, P., Wolf, K., and Lammerding, J. (2016). Nuclear envelope rupture and repair during cancer cell migration. *Science (New York, NY)*.

Devos, D.P., Graf, R., and Field, M.C. (2014). Evolution of the nucleus. *Current opinion in cell biology* 28, 8-15.

Diez, D.C., Seybert, A., and Frangakis, A.S. (2006). Tilt-series and electron microscope alignment for the correction of the non-perpendicularity of beam and tilt-axis. *Journal of structural biology* 154, 195-205.

Ding, R., West, R.R., Morpew, D.M., Oakley, B.R., and McIntosh, J.R. (1997). The spindle pole body of *Schizosaccharomyces pombe* enters and leaves the nuclear envelope as the cell cycle proceeds. *Molecular biology of the cell* 8, 1461-1479.

Fischer, T., Rodriguez-Navarro, S., Pereira, G., Racz, A., Schiebel, E., and Hurt, E. (2004). Yeast centrin Cdc31 is linked to the nuclear mRNA export machinery. *Nature cell biology* 6, 840-848.

Frost, A., Elgort, M.G., Brandman, O., Ives, C., Collins, S.R., Miller-Vedam, L., Weibezahn, J., Hein, M.Y., Poser, I., Mann, M., *et al.* (2012). Functional repurposing revealed by comparing *S. pombe* and *S. cerevisiae* genetic interactions. *Cell* 149, 1339-1352.

Gonzalez, Y., Saito, A., and Sazer, S. (2012). Fission yeast Lem2 and Man1 perform fundamental functions of the animal cell nuclear lamina. *Nucleus* 3, 60-76.

Heath, I.B. (1980). Variant mitoses in lower eukaryotes: indicators of the evolution of mitosis. *International review of cytology* 64, 1-80.

Henne, W.M., Buchkovich, N.J., and Emr, S.D. (2011). The ESCRT pathway. *Dev Cell* 21, 77-91.

Hurley, J.H. (2015). ESCRTs are everywhere. *EMBO J* 34, 2398-2407.

- Jaspersen, S.L., and Winey, M. (2004). The budding yeast spindle pole body: structure, duplication, and function. *Annu Rev Cell Dev Biol* 20, 1-28.
- King, M.C., Lusk, C., and Blobel, G. (2006). Karyopherin-mediated import of integral inner nuclear membrane proteins. *Nature* 442, 1003-1007.
- Kremer, J.R., Mastronarde, D.N., and McIntosh, J.R. (1996). Computer visualization of three-dimensional image data using IMOD. *Journal of structural biology* 116, 71-76.
- Kubai, D.F. (1975). The evolution of the mitotic spindle. *International review of cytology* 43, 167-227.
- Liu, H.L., Osmani, A.H., and Osmani, S.A. (2015). The Inner Nuclear Membrane Protein Src1 Is Required for Stable Post-Mitotic Progression into G1 in *Aspergillus nidulans*. *PloS one* 10, e0132489.
- Mackay, D.R., Elgort, S.W., and Ullman, K.S. (2009). The Nucleoporin Nup153 Has Separable Roles in Both Early Mitotic Progression and the Resolution of Mitosis.
- Madhani, H.D. (2013). The frustrated gene: origins of eukaryotic gene expression. *Cell* 155, 744-749.
- Mastronarde, D.N. (2005). Automated electron microscope tomography using robust prediction of specimen movements. *Journal of structural biology* 152, 36-51.
- Mastronarde, D.N. (2008). Correction for non-perpendicularity of beam and tilt axis in tomographic reconstructions with the IMOD package. *Journal of microscopy* 230, 212-217.
- McCullough, J., Colf, L.A., and Sundquist, W.I. (2013). Membrane fission reactions of the mammalian ESCRT pathway. *Annual review of biochemistry* 82, 663-692.

- McCully, E.K., and Robinow, C.F. (1971). Mitosis in the fission yeast *Schizosaccharomyces pombe*: a comparative study with light and electron microscopy. *Journal of cell science* 9, 475-507.
- McDonald, K.L., and Auer, M. (2006). High-pressure freezing, cellular tomography, and structural cell biology. *BioTechniques* 41, 137, 139, 141 passim.
- Monroe, N., and Hill, C.P. (2015). Meiotic Clade AAA ATPases: Protein Polymer Disassembly Machines. *Journal of molecular biology*.
- Morita, E., Colf, L.A., Karren, M.A., Sandrin, V., Rodesch, C.K., and Sundquist, W.I. (2010). Human ESCRT-III and VPS4 proteins are required for centrosome and spindle maintenance. *Proc Natl Acad Sci U S A* 107, 12889-12894.
- Munoz-Centeno, M.C., McBratney, S., Monterrosa, A., Byers, B., Mann, C., and Winey, M. (1999). *Saccharomyces cerevisiae* MPS2 encodes a membrane protein localized at the spindle pole body and the nuclear envelope. *Molecular biology of the cell* 10, 2393-2406.
- Niepel, M., Strambio-de-Castillia, C., Fasolo, J., Chait, B.T., and Rout, M.P. (2005). The nuclear pore complex-associated protein, Mlp2p, binds to the yeast spindle pole body and promotes its efficient assembly. *The Journal of cell biology* 170, 225-235.
- Olmos, Y., Hodgson, L., Mantell, J., Verkade, P., and Carlton, J.G. (2015). ESCRT-III controls nuclear envelope reformation. *Nature* 522, 236-239.
- Raab, M., Gentili, M., de Belly, H., Thiam, H.R., Vargas, P., Jimenez, A.J., Lautenschlaeger, F., Voituriez, R., Lennon-Dumenil, A.M., Manel, N., *et al.* (2016). ESCRT III repairs nuclear envelope ruptures during cell migration to limit DNA damage and cell death. *Science* (New York, NY).

Tallada, V.A., Tanaka, K., Yanagida, M., and Hagan, I.M. (2009). The *S. pombe* mitotic regulator Cut12 promotes spindle pole body activation and integration into the nuclear envelope. *The Journal of cell biology* 185, 875-888.

Tamm, T., Grallert, A., Grossman, E.P., Alvarez-Tabares, I., Stevens, F.E., and Hagan, I.M. (2011). Brr6 drives the *Schizosaccharomyces pombe* spindle pole body nuclear envelope insertion/extrusion cycle. *The Journal of cell biology* 195, 467-484.

Ulbert, S., Antonin, W., Platani, M., and Mattaj, I.W. (2006). The inner nuclear membrane protein Lem2 is critical for normal nuclear envelope morphology. *FEBS letters* 580, 6435-6441.

Vietri, M., Schink, K.O., Campsteijn, C., Wegner, C.S., Schultz, S.W., Christ, L., Thoresen, S.B., Brech, A., Raiborg, C., and Stenmark, H. (2015). Spastin and ESCRT-III coordinate mitotic spindle disassembly and nuclear envelope sealing. *Nature* 522, 231-235.

Webster, B.M., Colombi, P., Jager, J., and Lusk, C.P. (2014). Surveillance of nuclear pore complex assembly by ESCRT-III/Vps4. *Cell* 159, 388-401.

Witkin, K.L., Friederichs, J.M., Cohen-Fix, O., and Jaspersen, S.L. (2010). Changes in the nuclear envelope environment affect spindle pole body duplication in *Saccharomyces cerevisiae*. *Genetics* 186, 867-883.

Yang, D., Rismanchi, N., Renvoise, B., Lippincott-Schwartz, J., Blackstone, C., and Hurley, J.H. (2008). Structural basis for midbody targeting of spastin by the ESCRT-III protein CHMP1B. *Nat Struct Mol Biol* 15, 1278-1286.

Figure Legends

Figure 1. *vps4Δ* cells grow slowly, and loss of either *cmp7* or *lem2* rescues growth. (A)

Tetrad dissection of *vps4Δ/+* diploids, with genotypes labeled below the image. (B) Spontaneous suppressors (arrowhead) of *vps4Δ* (arrow) appearing after three days on rich media, with colony sizes comparable to those of wild type (*wt*) cells. (C) Growth curves of each genotype showing optical densities of yeast cultures, starting at OD_{600nm} 0.06, for 32 hours in 2-hour intervals. Three independent isolates for each genotype were measured. Here, and throughout, the plots show mean±SEM.

Figure 2. *vps4Δ* cells have severe nuclear envelope defects, which are suppressed by

loss of *cmp7* or *lem2*. (A) *wt* cells, showing normal NE morphologies (Ish1p-mCherry) and DNA (Hoechst staining) within the nuclei. (B) *vps4Δ*, showing various NE morphology defects including excess NE, fragmented NE, and DNA that appears to be outside of the nucleus. (C) Deletion of either *cmp7* or *lem2* rescues these NE morphology defects. Here and throughout, three independent isolates/strains were imaged for each genotype, and n represents the total number of scored cells. *wild type*: 1±1%, n=115, 121, 139; *vps4Δ*: 85±5%, n=62, 69, 86; *cmp7Δ*: 2.0±0.4%, n=151, 166, 147; *vps4Δcmp7Δ*: 1.1±0.7%, n =161, 118, 145; *lem2Δ*: 8±3%, n= 131, 103, 128; *vps4Δlem2Δ*: 12.2±0.7%, n=99, 176, 111. Two-tail student *t* tests were used here and throughout and designated as follows: **p*<0.05 , ***p*<0.01, ****p*<0.001, NS “Not Significant”. The scale bar represents 5 μm.

Figure EV1. *vps4Δ* and *lem2Δ* exhibit asymmetric SPB segregation. (A) *wt* cells showing

symmetric SPB segregation. (B) *vps4Δ* showing asymmetric SPB segregation. (C) Quantified percentages of asymmetric SPB segregation events in each genotype. Cells with septa were

selected and scored for SPB separation patterns. Nuclei were stained with Hoechst. *wt*: $0.7 \pm 0.3\%$, $n=103, 101, 101$; *vps4Δ*: $29 \pm 7\%$, $n=88, 103, 107$; *cmp7Δ*: $2 \pm 1\%$, $n=105, 103, 101$; *vps4Δcmp7Δ*: $4 \pm 2\%$, $n=117, 100, 104$; *lem2Δ*: $18 \pm 1\%$, $n=102, 103, 100$; *vps4Δlem2Δ*: $18 \pm 4\%$, $n=102, 103, 101$. The scale bar represents 5 μm .

Figure 3. *vps4Δ* cells display a series of mitotic defects associated with failure of nuclear membrane maintenance. (A) Time lapse of normal mitotic karyokinesis in *vps4Δ* cells. In all cases, the nuclear membrane is marked by Ish1p-mCherry and the SPB is marked by Cut12p-YFP. The total length of time is 100 minutes. (B) Karmellae formation correlates with defective separation of duplicated SPB. The total length of time is 400 minutes. (C) Asymmetric nuclear division. Total length of time is 100 minutes. (D) Failed nuclear division. Total length of time is 100 minutes. (E) Quantification of NE morphology during mitosis in *wt* and *vps4Δ*. Normal mitotic nuclear division, *wt*: $99 \pm 1\%$, *vps4Δ*: $27 \pm 8\%$; Karmellae formation, *wt*: 0% , *vps4Δ*: $29 \pm 3\%$; Asymmetric nuclear division, *wt*: $1 \pm 1\%$, *vps4Δ*: $38 \pm 2\%$; Failed nuclear division, *wt*: 0% , *vps4Δ*: $6 \pm 2\%$. *wt*, $n=23, 21, 18$; *vps4Δ*, $n=43, 51, 84$. Scale bars represent 5 μm .

Figure EV2. SPB separation is delayed in *vps4Δ* mutants. 16-hours time-lapse imaging (10 minute intervals) was conducted on *wt* and *vps4Δ* cells at 32°C, and the times required for SPB separation scored. Data were binned and plotted by mean frequency \pm SEM. *wt*: 10 minutes $96 \pm 2\%$; 20-50 minutes $4 \pm 2\%$; >50 minutes 0% ; $n=23, 22, 22$; *vps4Δ*: 10 minutes $57 \pm 4\%$; 20-50 minutes $31 \pm 4\%$; >50 minutes $12 \pm 3\%$; $n=30, 30, 30$.

Figure 4. *vps4Δ* cells have leaky nuclei and nuclear integrity is restored by loss of either *cmp7* or *lem2*. (A) GFP signals in the nuclear lumen of *wt* cells expressing NLS-GFP-LacZ. (B) *vps4Δ* cells expressing NLS-GFP-LacZ with moderate (arrowheads) or severe (arrow) nuclear leaking. (C) Percentages of cells with NLS-GFP-LacZ in the cytoplasm. *wt*: 0%, n=186, 116, 170; *vps4Δ*: 27±3%, n=130, 194, 217; *cmp7Δ*: 0.5±0.5%, n=125, 163, 132; *vps4Δcmp7Δ*: 4±1%, n=141, 127, 207; *lem2Δ*: 5±0.1%, n=113, 142, 148; *vps4Δlem2Δ*: 3±1%, n=167, 143, 125. The scale bar represents 10 μm.

Figure EV3. Time-lapse analysis of NLS-GFP-LacZ localization in *vps4Δ*. (A) Time-lapse images showing normal nuclear localization of NLS-GFP-LacZ converting to partial cytoplasmic localization. A pair of newly divided cells is shown over a time course of 100 minutes with 10-minute interval. (B) Time lapse images showing normal nuclear localization of NLS-GFP-LacZ converting to a homogenous distribution throughout the cell. A single cell is shown over a time course of 100 minutes with 10-minute interval. Scale bars represent 5 μm.

Figure 5. *vps4Δ* nuclear envelopes have persistent fenestrations, karmellae and disorganized tubular extensions. (A) Single tomographic slice showing the *wt* NE (left). NPCs are marked by asterisks. Segmented NE (green) with NPCs (red) reconstructed from 150 tomographic slices shown in a merged view (middle left), a front view (middle right) and a side view (right). (B) Single tomographic slice showing the *vps4Δ* NE (right). The following features and defects are highlighted: a fenestration (bracket), an NPC (asterisk), karmellae layers (white arrowheads), and a disorganized whorl of tubules (arrows). Segmented model of NE reconstructed from 100 tomographic slices is shown in a merged view (left) with karmellae in gold and a whorl of tubules in purple. (C) A segmented model of *vps4Δ* NE reconstructed from 200 tomographic slices is shown from the front (left), back (middle left), top (middle right) and bottom (right). (D) Single *vps4Δ* tomographic slice showing NPCs are absent from karmellae

region. The following features and defects are highlighted: a fenestration (bracket), an NPC (asterisk), and karmellae layers (white arrowheads). Segmented NE (green) with NPCs (red) and SPB (yellow) reconstructed from 150 tomographic slices shown in a merged view (middle left), a front view (middle right) and a side view (right). Scale bars in all panels represent 200 nm.

Figure EV4. Karmellae and tubular extension are connected NE structures in *vps4Δ*.

Selected tomographic slices of *vps4Δ* showing connected karmellae and tubular extensions. The relevant membranes are shaded light green and the junction is marked by black arrows. Scale bar applies to all panels and represents 200 nm.

Movie EV1: Segmented model of wild type NE from 150 tomographic slices. Color codes match Fig 5A

Movie EV2: Segmented model of *vps4Δ* NE from 100 tomographic slices. Color codes match Fig 5B.

Movie EV3: Segmented model of *vps4Δ* NE from 200 tomographic slices. Color codes match Fig 5C.

Movie EV4: Segmented model of another *vps4Δ* NE from 150 tomographic slices. Color codes match Fig 5D.

Figure 6. *vps4Δ* nuclear envelopes have persistent fenestrations, karmellae and disorganized extensions, and these defects are suppressed by loss of *cmp7* or *lem2*. (A) *wt* cells exhibiting normal NE. (B-D) *vps4Δ* cells showing a variety of NE phenotypes, including karmellae (B), multiple holes (arrows) (C), and discontinuities (black arrow head) that can contain NPCs (arrowheads) (D). (E and G) *cmp7Δ* and *lem2Δ* single mutants showing normal

NE morphology. (F and H) Double mutants showing that *cmp7Δ* and *lem2Δ* suppressed karmellae formation of *vps4Δ*. Scale bars represent 500 nm.

Figure 7. LEM2 or CHMP7 depletion in mammalian cells prevents recruitment of ESCRT-III to chromatin discs for role in nuclear formation at anaphase. (A) Schematic showing the experimental timeline used to enrich HeLa cells at anaphase. (B) Immunoblots showing LEM2 and CHMP7 depletion by independent oligos. (C) Quantification of IST1 recruitment to chromatin discs at anaphase B. Images acquired by widefield microscope were used for blind scoring of robust, weak, or no chromatin-associated IST1 foci. Statistical analyses were performed for the category of robust IST1 recruitment, comparing the siControl dataset to each depletion condition dataset siControl: 63±6%, n=18, 58, 24; siLEM2-1: 0±0%, n=40, 44, 12; siLEM2-2: 6±6%, n=34, 22, 6; siCHMP7-1: 0±0%, n=42, 20, 12; siCHMP7-2: 0±0%, n=22, 20, 2. (D) Confocal images illustrating IST1 localization in anaphase B cells under different conditions. Scale bar represents 10 μm.

Tables

Table EV1: Spontaneous suppressor alleles of *vps4Δ* identified in this study

Appendix Table S1: Yeast strains constructed for this study

Figures

Figure 1

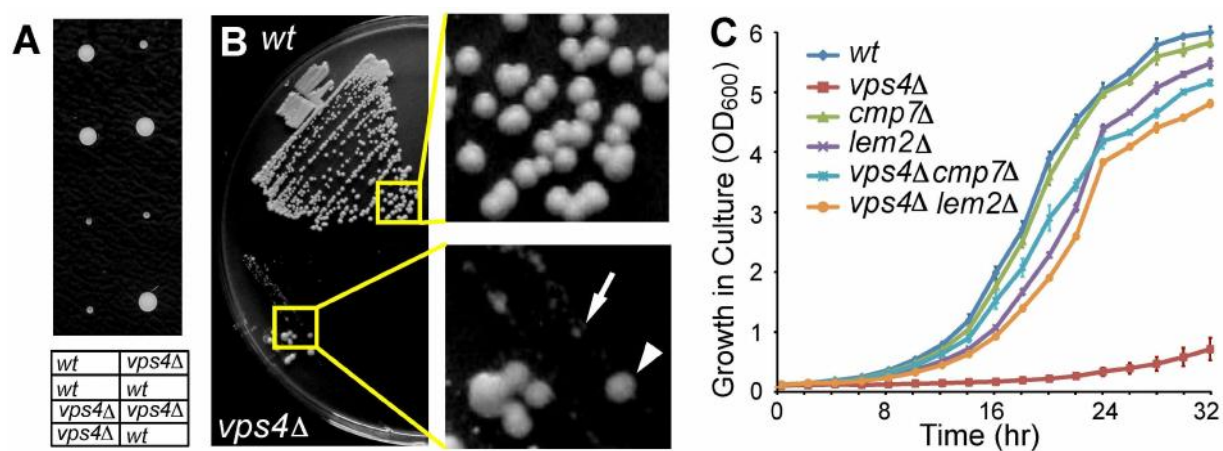


Figure 2

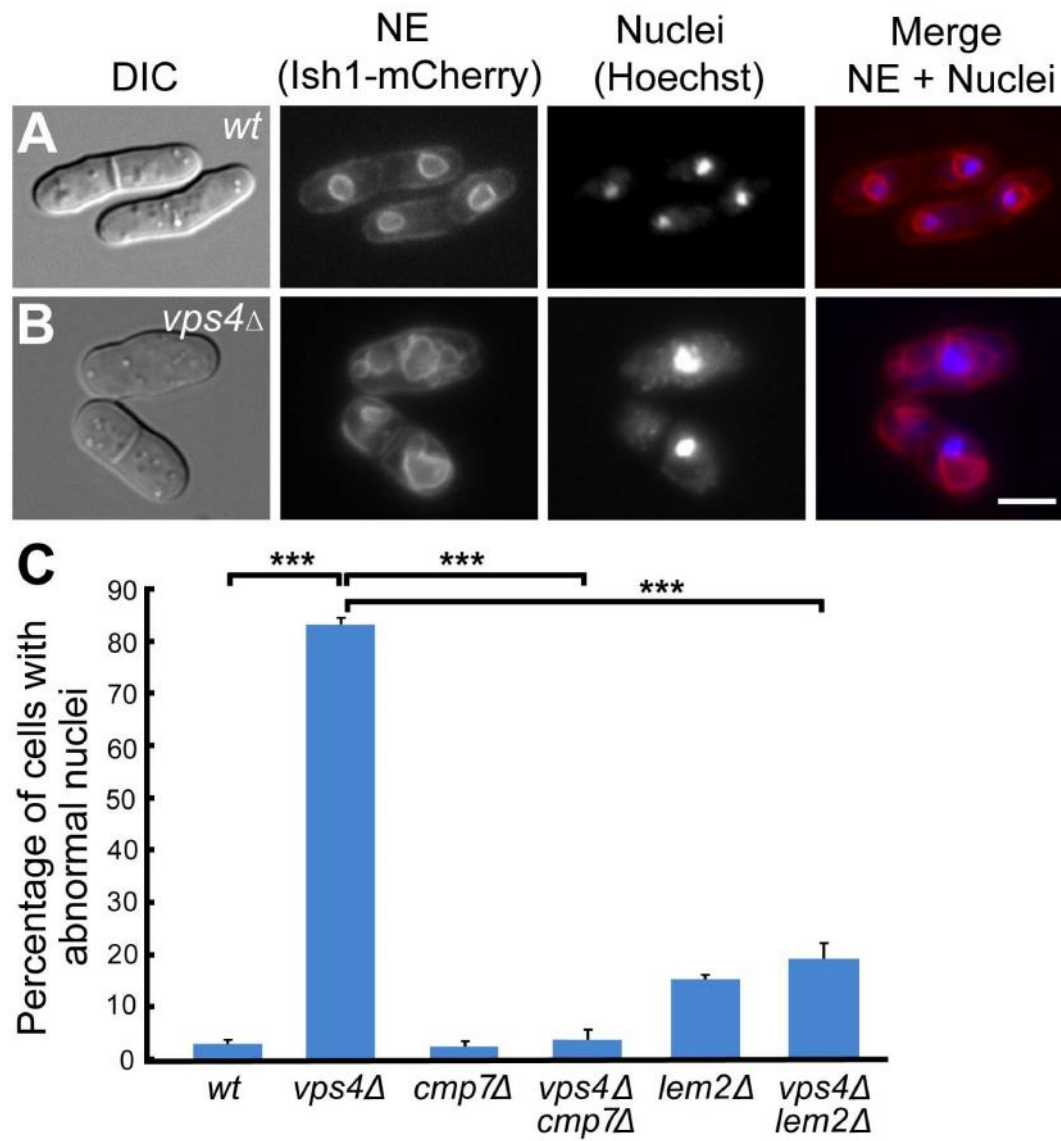


Figure EV1

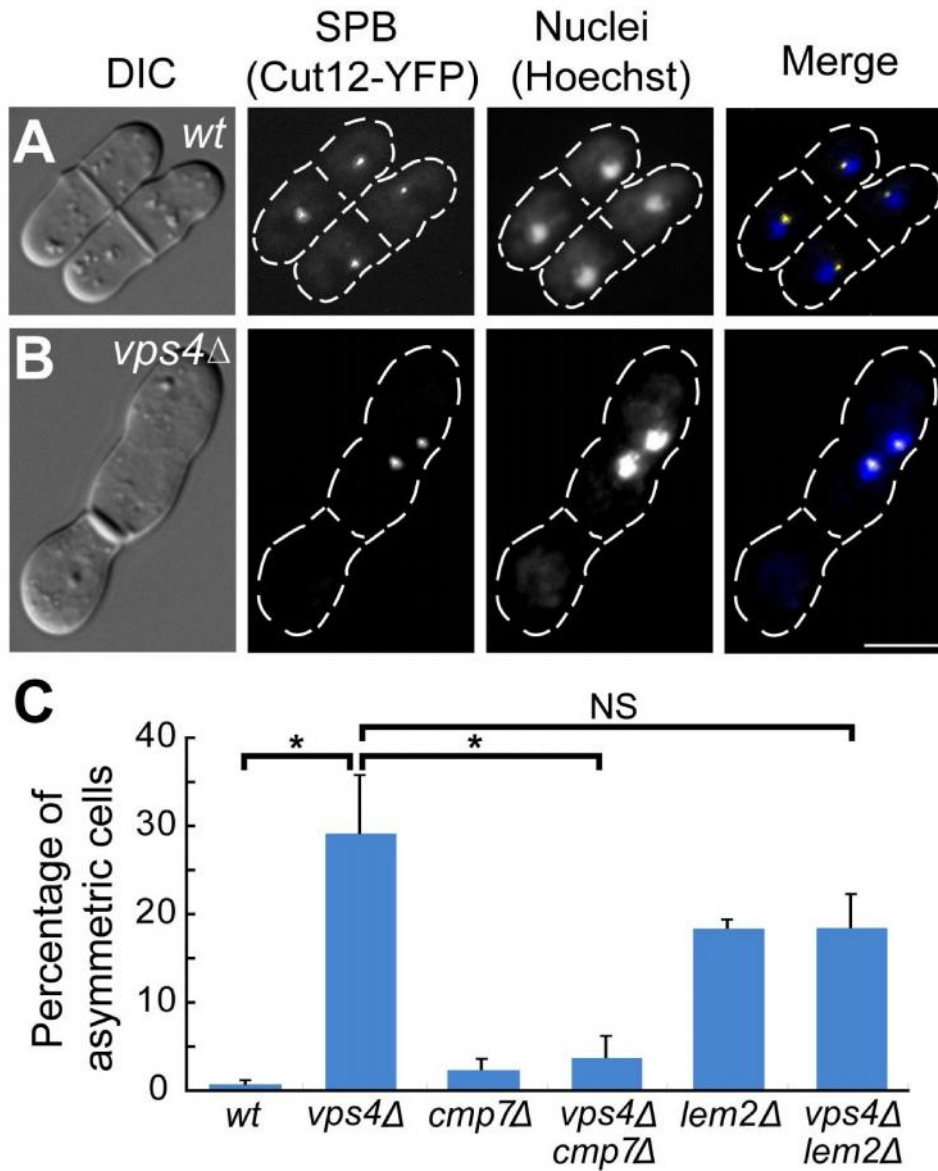
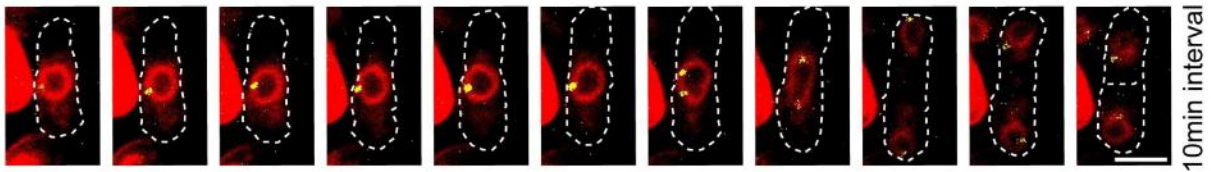
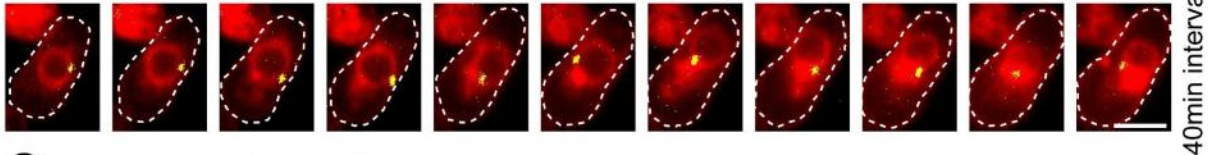


Figure 3

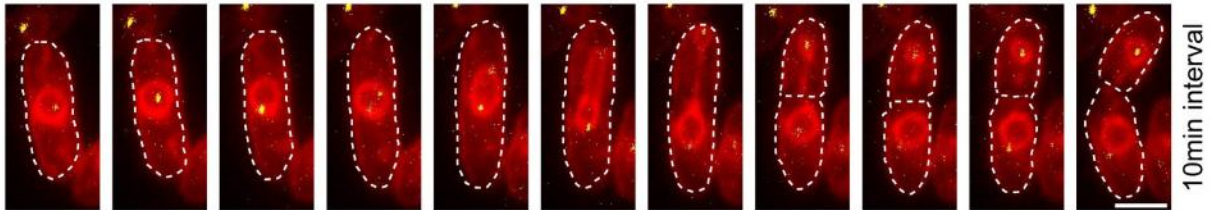
A Normal mitotic nuclear division



B Karmellae formation



C Asymmetric nuclear division



D Failed nuclear division

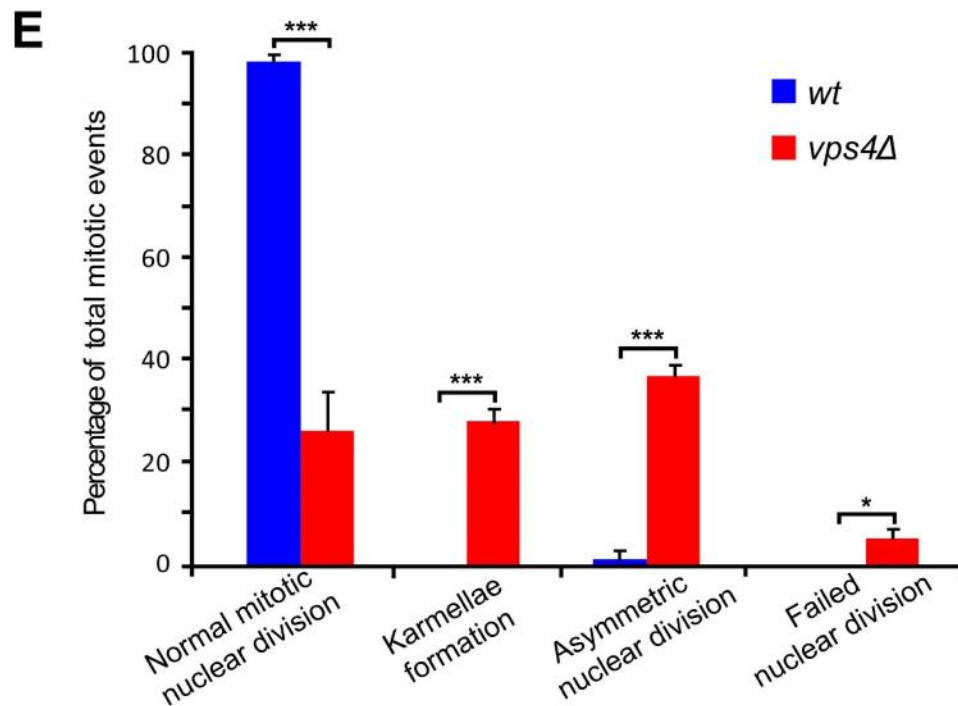
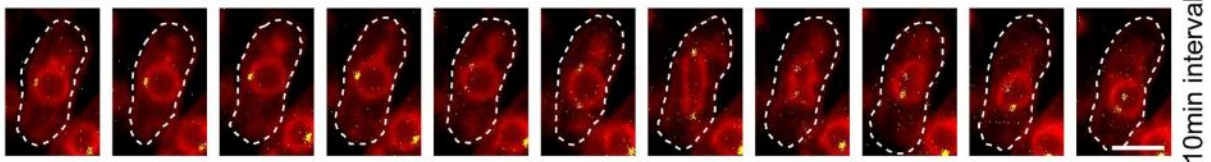


Figure EV2

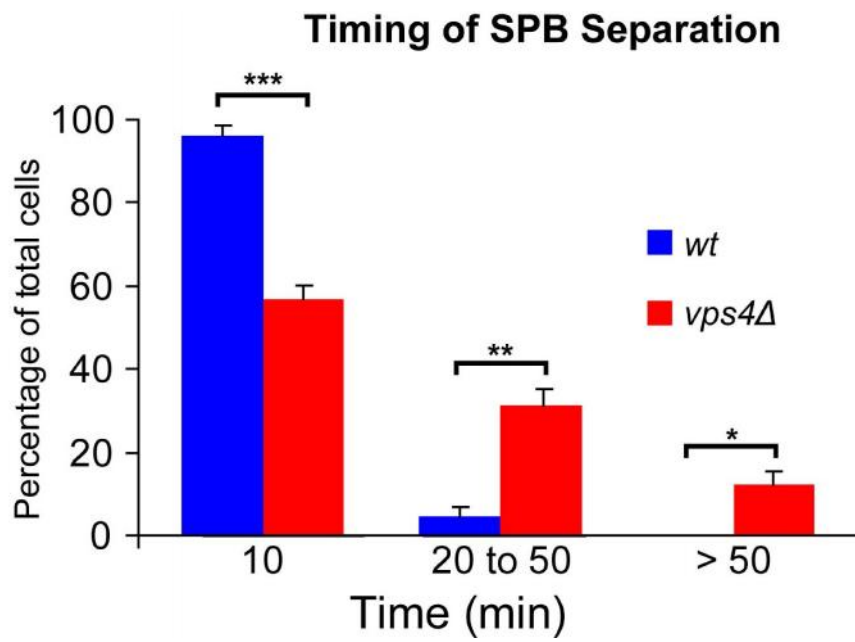


Figure 4

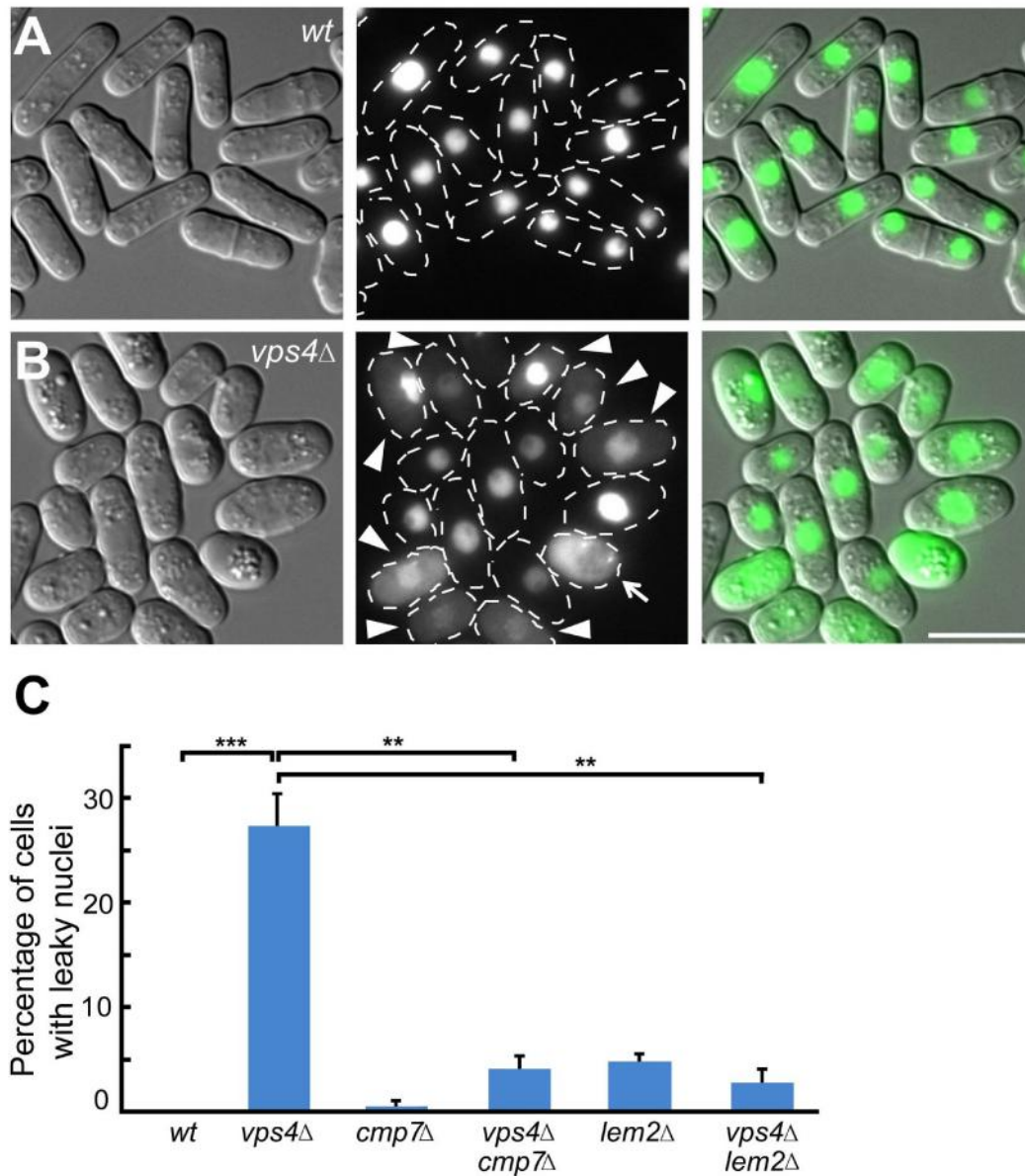


Figure EV3

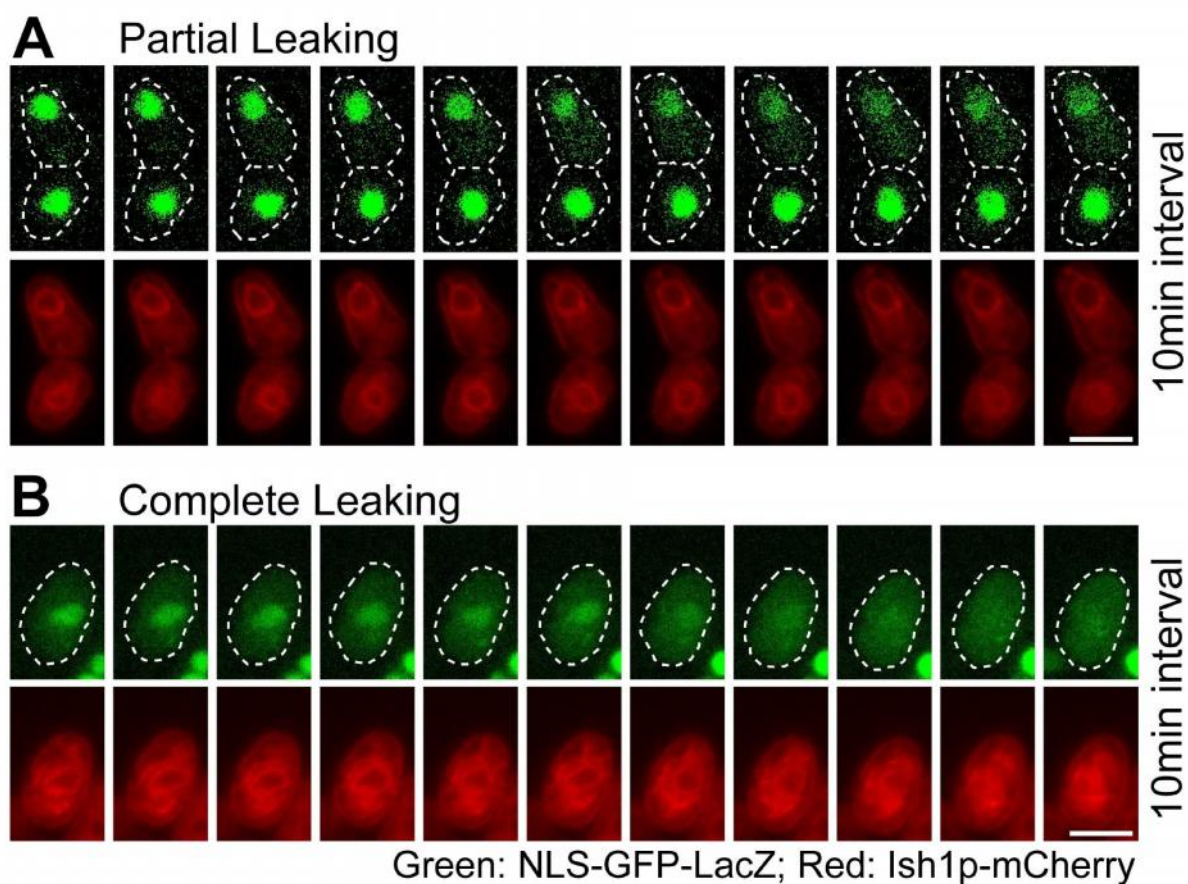


Figure 5

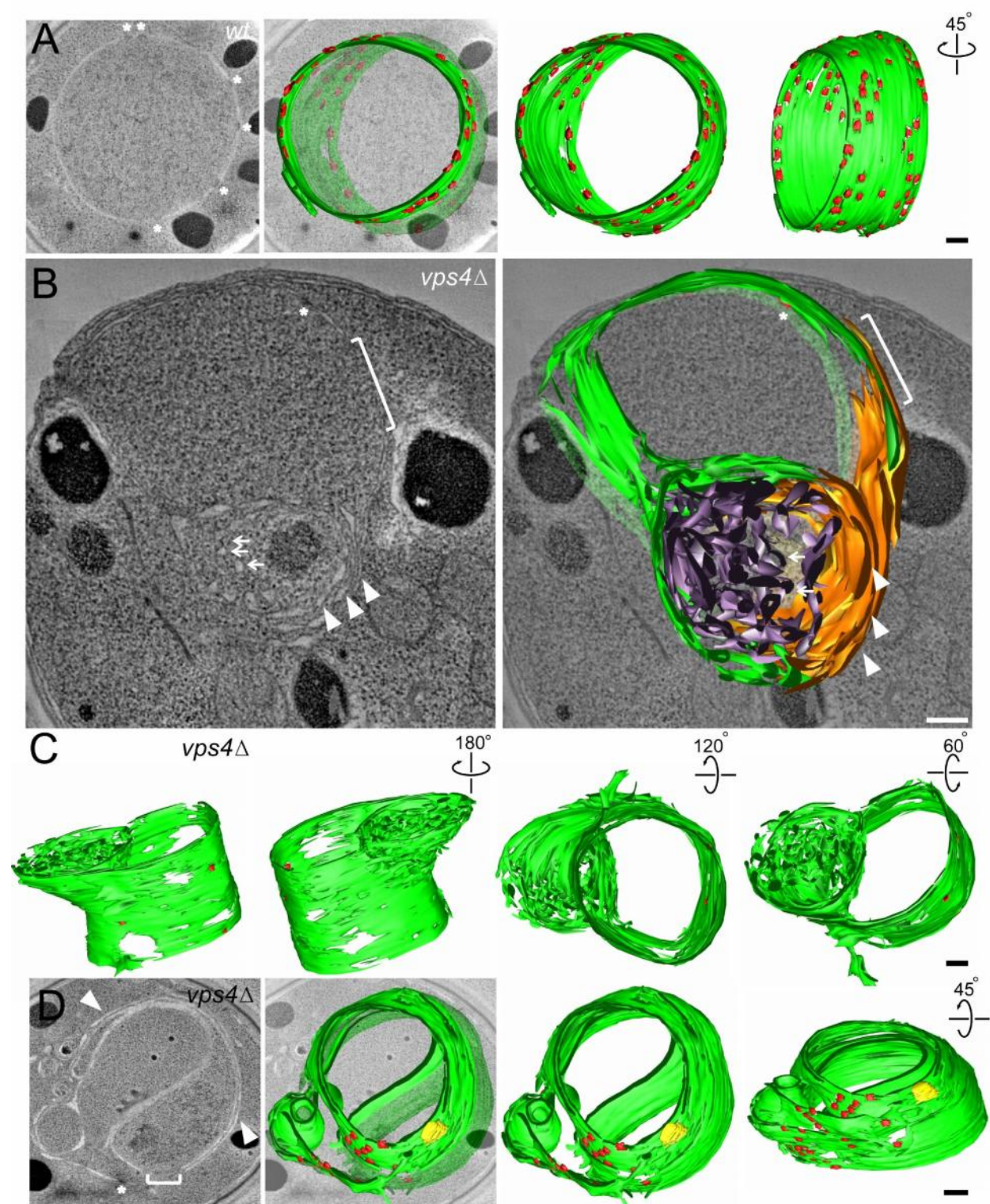


Figure EV4

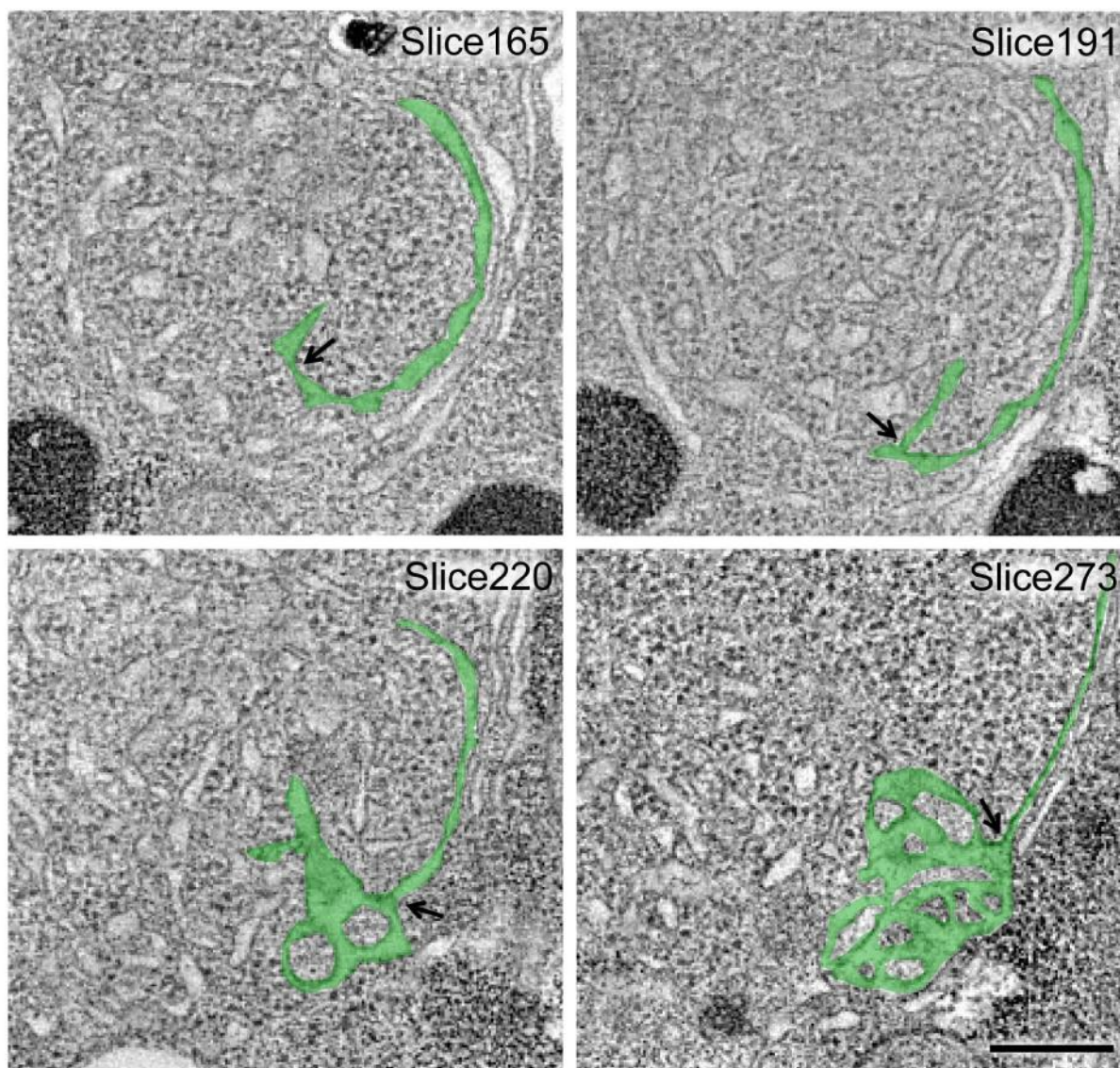


Figure 6

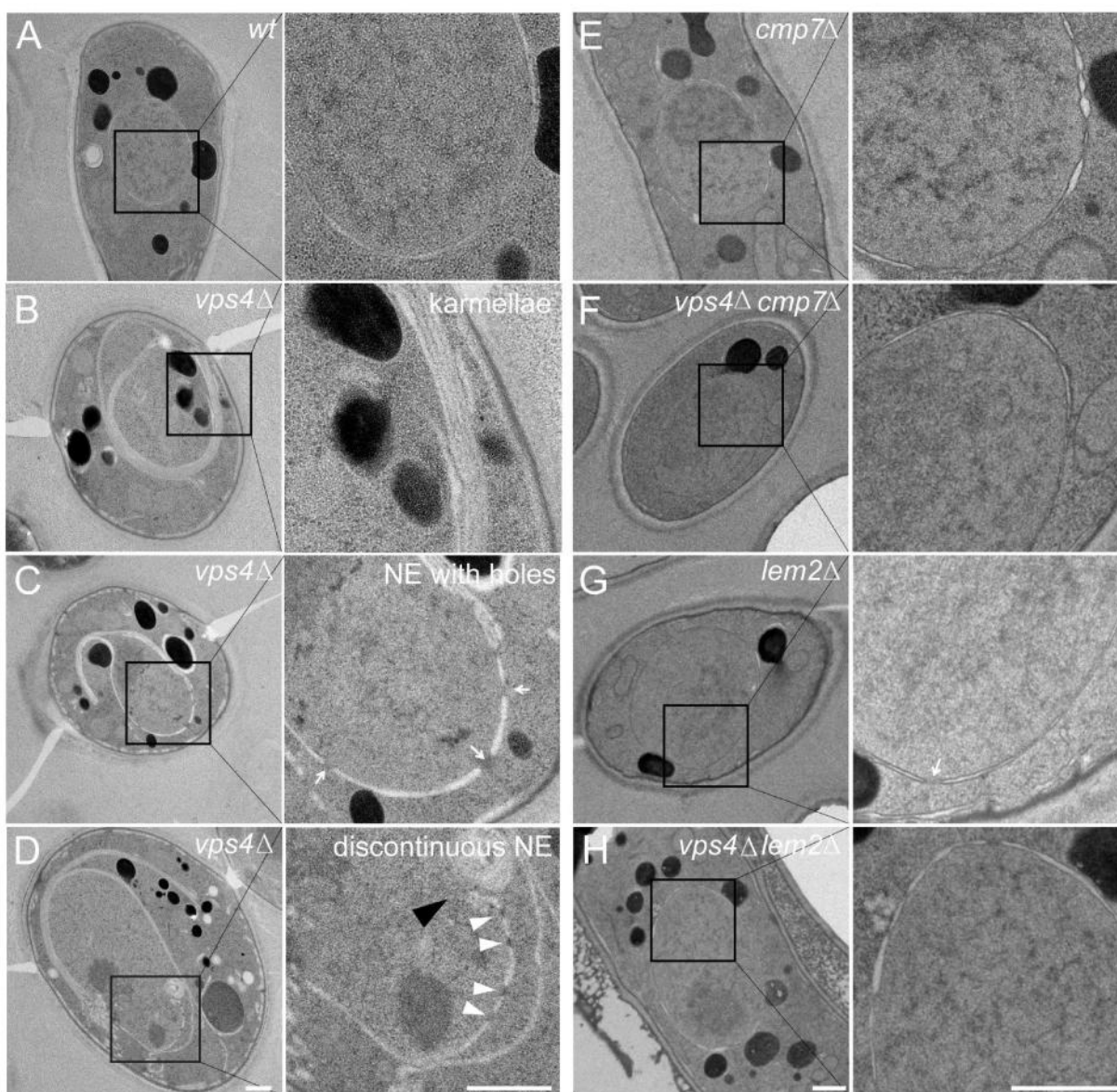


Figure 7

